New insights into the physics of agglomeration in solid propellants

Thomas Geoffrey Decker, Robin William Devillers, Stany Gallier

New insights into the physics of agglomeration in solid propellants

Thomas Geoffrey Decker[⋆]†, *Robin William Devillers*[⋆] *and Stany Gallier*[⋆⋆]
[⋆]*DMPE, ONERA, Universite Paris Saclay, Palaiseau, F-91123*
thomas.decker@onera.fr · robin.devillers@onera.fr
[⋆⋆]*ArianeGroup SAS, 9 Rue Lavoisier, 91710 Vert-le-Petit, France*
stany.gallier@ariane.group
†Corresponding author

Abstract

Shadowgraphy images of inert particles agglomeration in solid propellants are presented. New algorithms are developed and applied on three solid propellant compositions burning at a wide variety of pressures. Quantitative data focusing on the adhesive force applied by the propellant and the drag force applied by the gas flow on the particles are presented and discussed. The influence of pressure and oxidizing particles granular distribution is extensively investigated. Models of the adhesive the drag forces are proposed considering the experimental observations. The study offers new experimental and modeling perspectives and gives new insights into the complex physics of agglomeration.

1. Introduction

Solid Rocket Motors (SRM) are widely used in civilian and military applications. They require little maintenance, are highly reliable and readily available. A solid propellant is a solid material used to generate thrust by its combustion. It is composed of a fuel binder, usually Hydroxyl-Terminated PolyButadiene (HTPB) and oxidizing particles, usually Ammonium Perchlorate (AP). Metal particles, usually aluminum, are often added to increase the propulsion performances with additional combustion heat release [1].

The fuel binder and the oxidizing particles burn together at the propellant surface while the aluminium burns further off in the produced gas flow. Prior to its combustion, the aluminum particles agglomerate on the burning surface due to multiple complex physical phenomena: accumulation, adhesive force, drag force, ignition, etc. [2–4]. Agglomeration results in aluminum droplet size much bigger than the particles initially introduced. Predict the resulting droplet size is a key objective for the study of SRM stability [5–7] and performance [8–10].

Several numerical agglomeration models have been established [11–13], based on agglomeration data [14, 15] and experimental visualisations [16, 17]. Some agglomeration models contain a drag force expulsion criteria [18, 19], but use questionable hypotheses and modeling. No model contains a complete physics of agglomeration, due to the lacking quantitative data on the retention force applied by the burning surface and the drag force applied by the gas flow. The two forces have opposite effects and the aluminum ejection depends on their balance [16].

The specific study of those two forces with aluminum loaded solid propellants is complex due to the overwhelming effect of aluminum ignition and coalescence [2, 20], as well as the produced smoke which hinders visualization [20]. Adding inert particles instead of aluminum particles is a first good way to focus on the aluminum-related agglomeration phenomena not totally understood and an interesting first stage before moving to aluminum. Some image processing algorithms have already been developed [21–23]. However, quantitative data on parameters influencing the adhesive and drag forces, such as pressure or solid propellant composition, are yet to be published.

This article focuses on the agglomeration of three different solid propellant compositions loaded with inert particles at several pressures. Quantitative data on the particles behavior on the solid propellant surface and in the gas flow are measured and discussed. Some physical quantifiers are also calculated in order to further discuss the influence of the solid propellant granular distribution. The physics associated to the particle agglomeration is investigated. Adhesive and drag force modeling are proposed.

2. Experimental & Numerical materials

2.1 Experimental setup & solid propellant compositions

A shadowgraphy set-up is used to visualize the particle agglomeration on the propellant surface and in the gas flow. The set-up is highly efficient for inert particle visualization due to the absence of oxide smoke production by aluminum combustion [21, 22, 24]. It is essentially made of a extended visible light source focused on the propellant sample. The samples mass is less than one gram. They are placed in a combustion chamber pressurized with inert gas, the chamber can be pressurized up to 30 bar, but visualizations have been focused here below 16 bar. A 7500 Hz high-speed camera and extremely precisely placed imaging optics enable the acquisition of sharp images at a high frame rate with a fine spatial resolution of approximately 3 $\mu m/px$. The ignition of the solid propellant sample is realized with a 2 kW CO_2 laser. The sample is quickly ignited, resulting in a planar burning surface. Figure 1 shows the shadowgraphy set-up. Figure 2 shows a shadowgraphy image of a solid propellant combustion showing inert particles ejected in the gas flow.

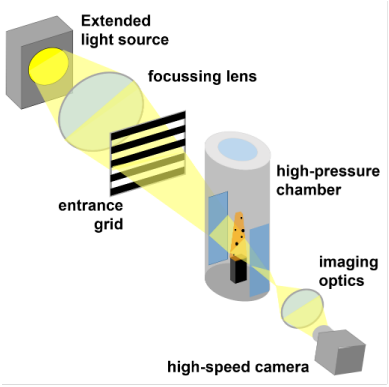

Figure 1: Shadowgraphy set-up [21].

Figure 2: Example of a shadowgraphy image (2644 propellant at the pressure of 4.0 bar).

Three propellant compositions are studied. They differ in the granular distribution of the AP oxidizing particles. They include the same amount of inert particles, 10%$_m$ of ceramic particles with a representative diameter D_{10} of 41.6 μm. The propellant composition is presented in table 1. The propellant 2646 includes the largest proportion of coarse and medium AP, while the propellant 2645 only contains medium and fine AP. The initial pressure in the combustion chamber can be adjusted before ignition, enabling the study of several burning pressures for each propellant. Four pressures are studied for the 2644 and 2645 propellant, six for the 2646 propellant. This results to a total of fourteen experiments. The pressures studied are visible in figure 3.

Table 1: Propellants compositions (mass fraction).

Propellant	**Inert Particles**	**AP**			**Binder**
	B400 [41.6 μm]	Coarse [200 μm]	Medium [90 μm]	Fine [9 μm]	HTPB
2644	10%	55%	0%	55%	10%
2645	10%	0%	40%	40%	10%
2646	10%	30%	27%	16%	17%

The burning rate r_b is calculated for each run using a simple image processing algorithm with an image thresholding (the propellant is dark while the gas is bright, visible in figure 2). The averaged separating surface height is calculated over time. The burning rate is estimated as the slope from a linear regression on the average height. The burning rate r_b is modeled with a Vieille's law $r_b = AP^n$ for all three propellants. The exponent n equals about 0.5 for the 2644 and 2645 propellants, about 0.3 for the 2646 propellant. Figure 3 shows the calculated burning rates of all experimental runs studied, alongside the Vieille's law modeling. Horizontal error bars are the minimum and maximum pressure before and after the propellant combustion. Vertical error bars are the burning rate uncertainty associated to the surface detection uncertainty.

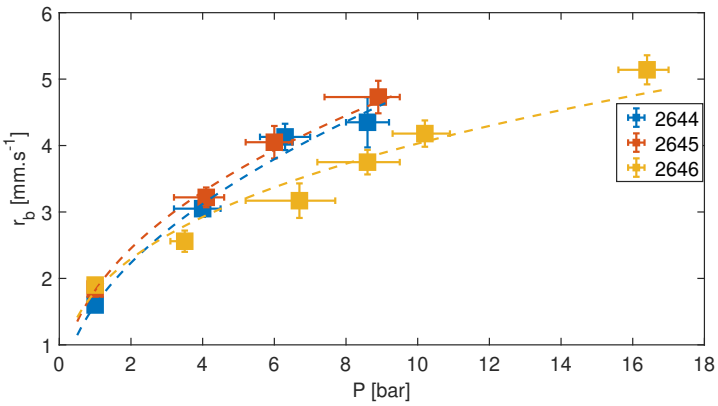

Figure 3: Burning rates at the various tested pressures.

2.2 Propellant packings

The three propellants are also studied numerically with packings in order to get insights into their geometrical structures. A packing is a numerical representation of a propellant as an ensemble of spheres, representing the granular composition. Every particle with sufficient size (i.e coarse and medium AP and inert particles) are placed in a periodic volume. Fine AP particles are homogenised with the binder as a pseudo-binder because of their small sizes. The algorithm used to place particles is based on Jodrey-Tory method [25]. All spheres are initially placed as points (no volume). The particle volumes progressively increases with each iteration until the targeted volume fraction is reached. It has been previously found that the geometric repartition of a packing and a real solid propellant are almost identical [26]. The packings of the three propellants studied can be visualised in figure 4, with inert particles represented in black. The smallest AP particles (smallest medium AP) are represented in red, the largest (largest coarse AP) in blue.

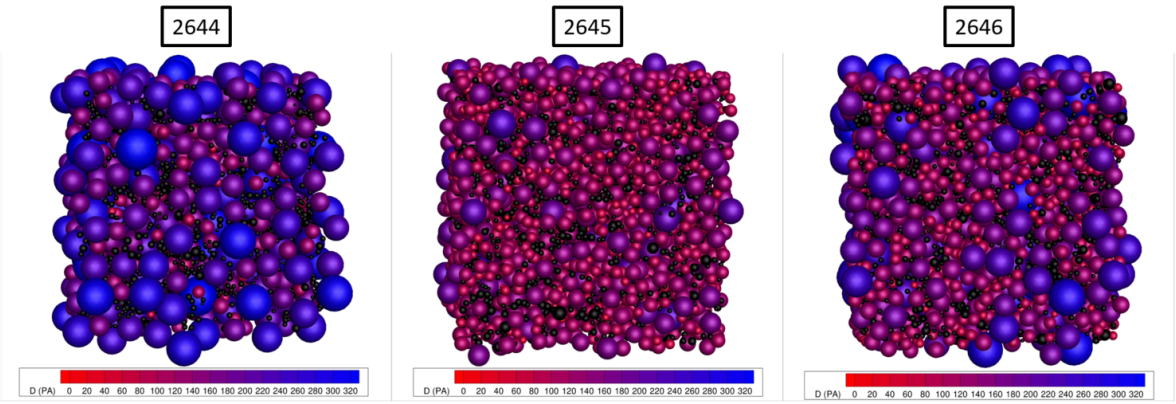

Figure 4: Packing of the three propellants. Inert particles are represented in black, the smallest AP particles in red, the largest in blue.

3. Computed data & results

The physics associated to the inert agglomeration is discussed in this section. Quantitative data of the agglomeration process are calculated in order to study the associated physical phenomena. The experimental data are obtained by image processing algorithms due to the large quantity of acquired images (14 runs, with up to 10000 images by run).

3.1 Adhesive force study

The first objective is to study the particles behavior on the burning surface and the formation of particle aggregates. Particles are retained to the burning surface by an adhesive force. Studying the particles and aggregates time evolution

on the burning surface is a way to investigate this force.

3.1.1 Surface detection & tracking

A surface detection is performed, using the Chan-Vese active contour [21, 27]. The detection of protruding particles and aggregates attached to the surface is performed based on the detected surface frontier. The ENC (Extreme of Normalized Curvature) surface description highlights the areas with strong curvature associated to the protruding particles and aggregates [23]. ENC is a multi-scale description that has been developed which enables the detection of all patterns with sufficient protuberance, even individual particles [23]. The detections are tracked on successive images using the IOU (Intersect over Union) metric [22]. Figure 5 shows an example of a tracked aggregate on the burning surface. When attached to the surface before being ejected in the gas flow, a particle becomes an aggregates if it sinters with at least one other particles, like in figure 5. It remains an individual particle otherwise.

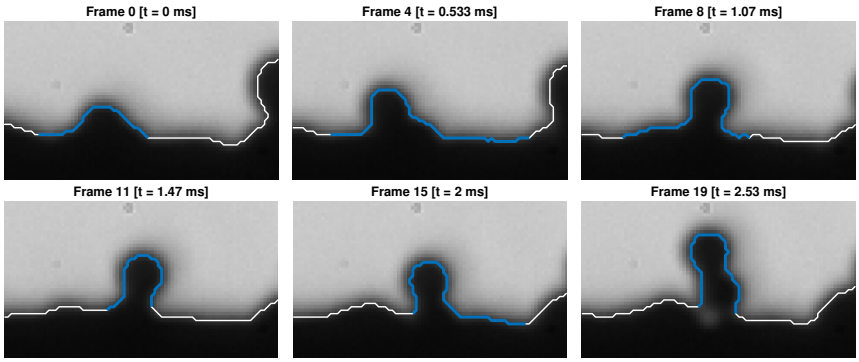

Figure 5: Example of a tracked aggregate formed by two particles.

3.1.2 Protuberance growth & vertical motion

The adhesive force is investigated with two time functions: the protuberance growth (i.e. the uncovering) of the protrusion and the vertical motion of the object. The protuberance is the portion of the particle/aggregate that protrudes out from the surface, showing their emergence. The protuberance h_{prot} is the protrusion height relative to the propellant surface. The upper position of the tracked object y_{top} is the point located on the highest position on the studied object. Examples are presented in figures 6 and 7.

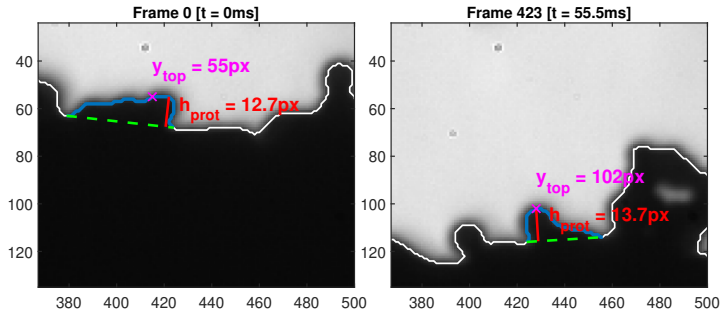

Figure 6: Protuberance h_{prot} and upper vertical position y_{top} for a totally stuck particle on the propellant surface.

The functions h_{prot} and y_{top} are calculated over time for each detection of an object. The time-evolution allows to delineate different particle/aggregate behaviors on the burning surface:

- If the object is completely stuck to the surface, the protuberance h_{prot} is constant. The vertical position goes downward following the surface regression.
- If the object is uncovered with the propellant combustion and partially free from the surface, the protuberance h_{prot} increases and the position y_{top} is constant.

A linear regression is performed on h_{prot} and y_{top}. The slopes are labeled a_h ($\approx \frac{dh_{prot}}{dt}$) and a_y ($\approx \frac{dy_{top}}{dt}$). Two dimensionless metrics N_h and N_y are calculated by normalizing the slope with the burning rate r_b:

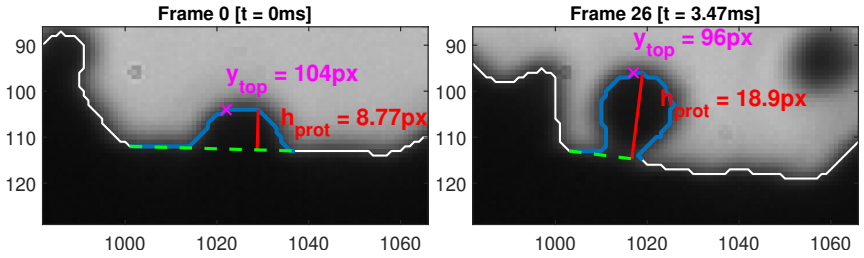

Figure 7: Protuberance h_{prot} and upper vertical position y_{top} for a lightly stuck particle on the propellant surface.

- $N_h = \frac{a_h}{r_b}$. $N_h \to 1$ means that the object becomes uncovered by the propellant sample regression, while $N_h \to 0$ means that the object is stuck to the surface.
- $N_y = \frac{a_y}{r_b}$. $N_y \to 1$ means that the object is stuck to the surface while $N_y \to 0$ means that the object becomes uncovered by the propellant sample regression.

N_h and N_y enable the characterization of the particle/aggregate adhesion behaviour to the burning surface. The two numbers are studied alongside to increase confidence with the behaviour characterized. Two examples are presented in figures 8 and 9. The functions and numbers N_h and N_y are calculated for the two tracks presented in figures 6 and 7. Two different behaviors are observed and are well characterized with the dimensionless numbers. For the totally attached particle (figures 6 and 8), N_h is close to 0 and N_y is close to 1. For the partially attached particle (figures 7 and 9), N_h is superior to 1 and N_y is close to 0.

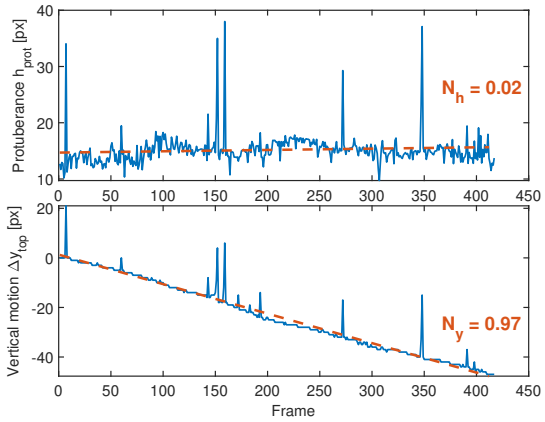

Figure 8: Time-evolution of the protuberance h_{prot} and the vertical displacement Δy_{top}, of the totally attached particle presented in figure 6.

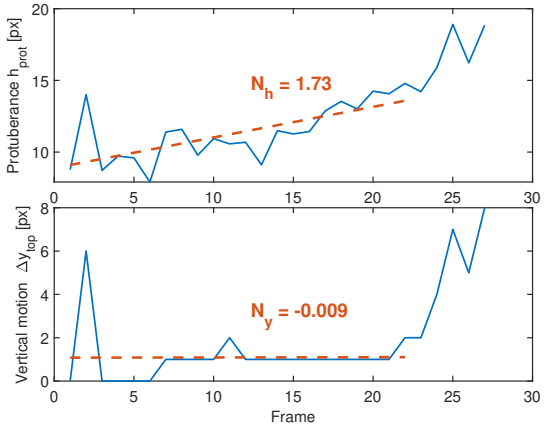

Figure 9: Time-evolution of the protuberance h_{prot} and the vertical displacement Δy_{top} of the lightly attached particle presented in figure 7.

3.1.3 Experimental result regarding adhesive effects

The median values of the dimensionless numbers N_h and N_y are calculated for each run. They are presented in figure 10. Error bars are the 25% and 75% values of the dimensionless numbers cumulative distribution.

A clear effect of the propellant composition is visible but there is no clear effect of pressure. The inert particles of the 2646 propellant are the less strongly stuck to the surface (largest N_h and lowest N_y), while the particles of the 2645 propellant are the most strongly stuck to (lowest N_h and largest N_y). The 2646 propellant includes the most coarse and medium AP particles, it is the opposite for the 2645 propellant. It suggests that the adhesive force is pseudo-binder related, i.e. induced by the binder and the fine AP particles surface layer. An inert particle has more chance to hit a larger AP particle if the coarse and medium AP volume fraction is important, and more chance as well to hit another inert particle due to the particles accumulation in pockets [13]. When an inert particle hit another inert particle, they form an aggregate through sintering (see figure 5), limiting the adhesion to the surface of the first particle. When an inert particle hit an oxidizing particle, it is believed that the inert particles are ejected in the gas flow [16], because the adhesion to the pseudo-binder surface is broken.

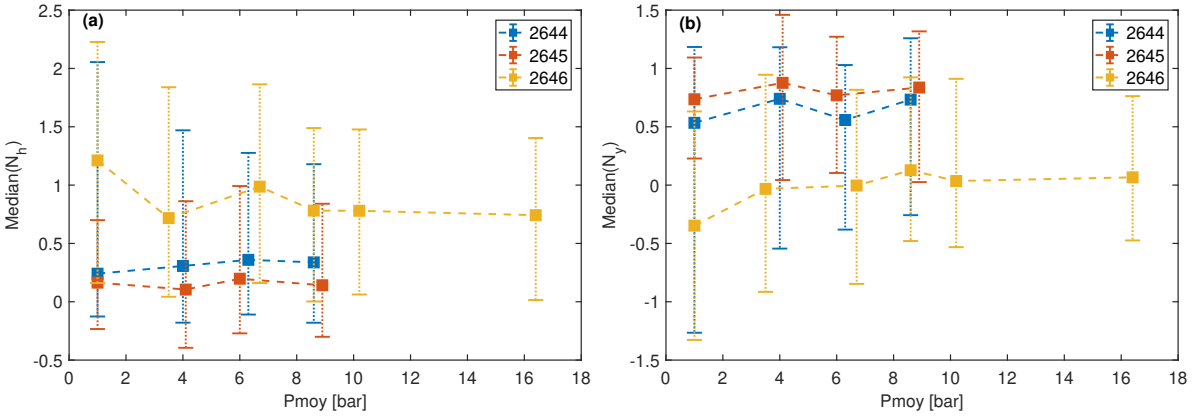

Figure 10: Median values of (a) N_h and (b) N_y at different pressures for the three propellants studied.

3.1.4 Propellant packs metrics

Numerical metrics are calculated for all propellant packs in order to validate the experimental observation just highlighted above for the adhesive behaviors. The granular repartition is studied. For all three propellants, the free vertical length for each inert particle is calculated. The free vertical length is the vertical distance before the particle collides with an oxidizing particle or another inert particle. It represents the potential vertical movement of an inert particle (IP) before hitting another particle. A schematic of the free vertical lengths are presented in figure 11.

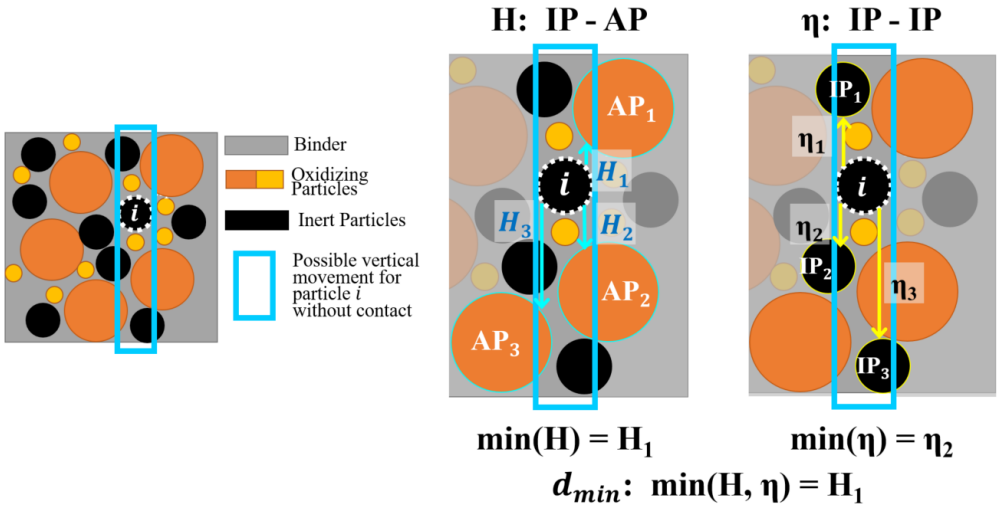

Figure 11: Schematic of the calculation of the free vertical distances for an inert particle i. On the left-hand side, the free distance H before colliding with a large oxidizing particle. On the right-hand side, the free distance η before colliding with another inert particle.

The free vertical distance is the maximal distance possible before an inert particle collides with an AP particle (IP-AP) or another inert particles (IP-IP). A large free distance leads to a longer residence time on the surface. The distances are calculated for all propellants packs inert particles, ≈ 5000. The median free vertical distances are presented in table 2. The 25% and 75% values of the free distance cumulative distributions are also presented. A strong disparity is observed. The experimental median values of the dimensionless number N_y are presented for comparison. Large N_y means that particles are stuck on the propellant surface, low N_y means that particles are uncovered with the propellant surface regression.

The median free distances confirm the observed experimental result. The 2646 is the propellant for which the inert particles have the most chance of colliding with other particles (low distance d_{min} values), thus limiting their total adhesion to the burning surface. A lightly-stuck behavior was observed for the 2646 inert particles in figure 10. The opposite can be said for the 2645 propellant where inert particles can stay attached to the surface on longer distances

Table 2: Granular median free vertical distances [μm].

	H		η		**d_{min}**		
Propellant	**50%**	25% – 75%	**50%**	25% – 75%	**50%**	25% – 75%	**N_y**
2644	**28.7**	11.9 – 62.1	**47.1**	14.5 – 151	**15.5**	6.2 – 31.0	**0.64**
2645	**26.9**	10.8 – 58.5	**77.5**	24.6 – 205	**17.9**	7.6 – 35.9	**0.80**
2646	**13.6**	5.8 – 29.0	**48.0**	15.1 – 154	**9.4**	3.8 – 18.6	**–0.03**

(large d_{min}) before colliding with other particles. A strongly-stuck behavior was observed for the 2646 inert particles in figure 10. The numerical metrics confirm that the propellant granulometry drives the particles behavior on the burning surface, and shows that the adhesive force is pseudo-binder related.

3.2 Drag force study

The second objective is to study the particles behavior in the gas flow once ejected. The ejection depends on the balance between the adhesive force applied by the propellant surface and the drag force applied by the gas flow. Once ejected, the particles accelerate in the gas. Studying the particles acceleration in the gas is a way to investigate the drag force.

3.2.1 Gas detection & tracking

Particles can be regrouped as aggregates or remain individual when they leave the surface and move in the gas flow. Objects (particles and aggregates) are detected in the gas flow using the MSER (Maximally Stable Extremal Regions) algorithm [28], which has been found effective in the past for similar shadowgraphy images [24]. A diameter value is estimated with the area detected by MSER and the blur of the object corrected using the Blaisot correction [29].

Individual particles are differentiated from aggregates. The properties used to classify the objects are their detected area and their aspect ratio. Manual annotations have been used to optimize the classification.. About 1000 detections per run have been manually annotated. A simple affine border in the (Area, Aspect Ratio) plane is used to discriminate the aggregates. 93% of detections are correctly classified for the specific run annotated. Over 90% of detections are correctly classified for other runs using the same separation line. An annotated image is presented in figure 12 with particles plotted in blue and aggregates plotted in red. Figure 13 shows the calculated separating line between particles and aggregates with the labeled detections plotted.

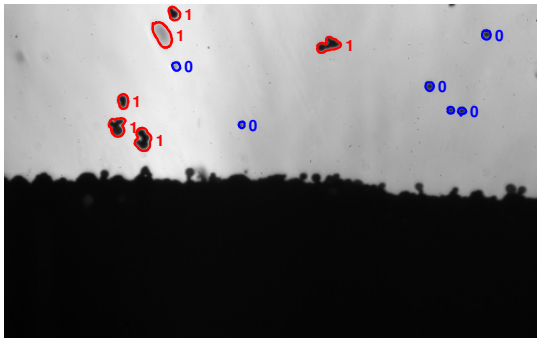

Figure 12: Example of annotated image (2644 propellant at 4.0 *bar*), non-processed image is presented in figure 2. Particles are labeled "0" and aggregates "1".

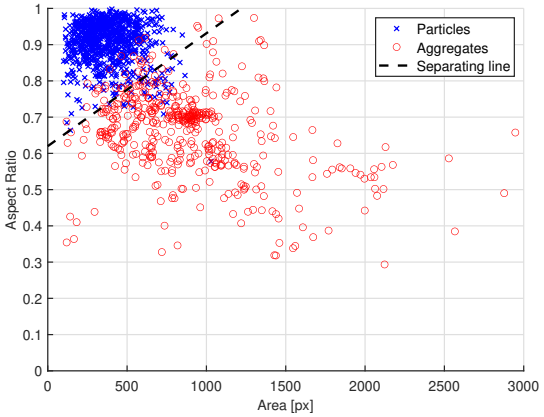

Figure 13: Calculated separating line between annotated particles and aggregates. With detections manually labeled as particle in blue and as aggregate in red.

Detections are tracked on successive images using a Kalman filter [30]. The diameter of the tracked object and its classification particle/aggregate are averaged on all the detections associated to this track to reduce the uncertainty. An example of a tracked aggregate in the gas flow is presented in figure 14.

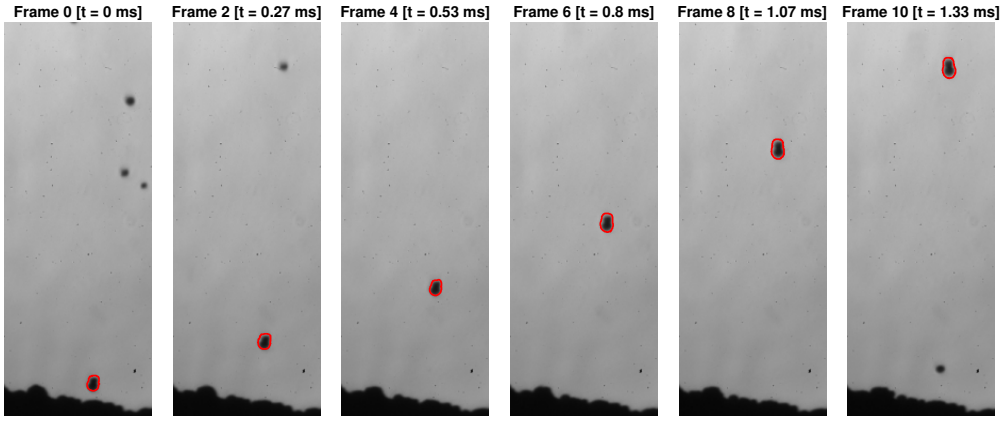

Figure 14: Example of a tracked aggregate in the gas flow (2644 propellant at 4 *bar*).

3.2.2 Particle acceleration calculation

The drag force is investigated with the particles acceleration. The gas flow applies a drag force F_d on the particles and aggregates. The Schiller-Naumann correction $C_D = \frac{24}{Re}(1 + 0.15Re^{0.687})$ is adapted for the particles with Reynolds between 0.1 and 1000, which is the case in this study. Aggregates acceleration is not studied in the present work due to their complex shape and the difficulty to model the drag coefficient C_D (aggregates related metrics are presented in section 4.1). The drag force applied by the gas flow to a particle is written:

$$F_d = \frac{1}{2}\rho_g C_D A(v_g - v_{part})^2 = m_{part} a_{th} \tag{1}$$

With ρ_g the gas density, A the cross sectional area, v_g and v_{part} the gas and particle velocities, m_{part} the particle mass and a_{th} the theoretical acceleration. Particle are usually tracked on a limited time of 10 successive frames, approx. $1.33ms$. The characteristic time τ of the velocity differential equation is $\tau = \frac{\rho_{part} D_{part}^2}{18\mu_g} \approx 6.6ms$. The resulting particle velocity at the end of a track v_{part} is considered negligible compared to the gas flow velocity v_g. Several additional assumptions are made:

- The gas velocity v_g is supposed constant, and can be approximated as $\frac{r_b \rho_{prop}}{\rho_g}$ (mass flux conservation at the propellant surface). With $r_b = AP^n$.
- The gas temperature is supposed constant: μ_g and ρ_g are constant.
- The gas is supposed ideal: $P = \rho_g r T_g$.

The theoretical acceleration for the particles is therefore written:

$$a_{th} = \frac{18\mu_g v_g}{\rho_{part}}(1 + 0.15Re^{0.687})\frac{1}{D_{part}^2} = \frac{18A\mu_g \rho_{prop} r T_g P^{n-1}}{\rho_{part}}(1 + 0.15Re^{0.687})\frac{1}{D_{part}^2} \tag{2}$$

The theoretical acceleration is used as a baseline. The hypotheses made are questionable, especially the constant gas temperature, since there are strong temperature gradients close to the burning propellant surface. The influence of the gas velocity, the particles diameter and the temperature will be discussed. The equilibrium thermodynamic properties of the gas flow (ρ_g, μ_g, T_g far from the propellant burning surface) are calculated with an in-house code for each experimental run. The theoretical acceleration is calculated for each tracked particle with the estimated diameter.

The experimental acceleration is supposed constant along the particle movement close to the surface like the theoretical one. Thus, the distance d of the particle from the burning surface can be written directly as a function of the experimental acceleration a_{expe}, the initial vertical velocity v_0, and the initial vertical position y_0 of the particle:

$$d = \frac{1}{2}a_{expe}t^2 + v_0 t + y_0 \tag{3}$$

The distance d is interpolated on the whole track for each particle, a_{expe}, v_0 and z_0 are hence calculated. An example of the distance function d and its interpolation is presented in figure 16, with the tracked particle displayed in figure 15. The experimental accelerations values are studied next. A drag force modeling is proposed in section 4.2 with the experimental observations highlighted.

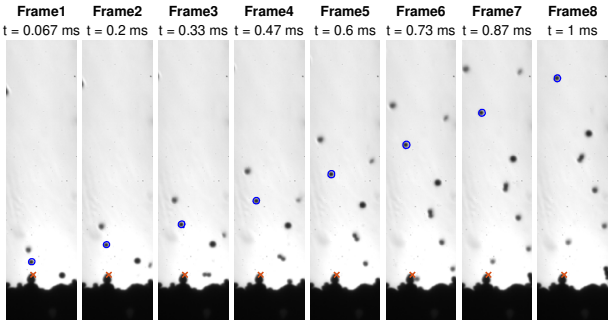

Figure 15: Example of a tracked particle (blue) with the vertical surface reference (orange cross).

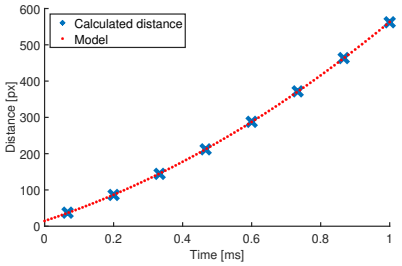

Figure 16: Vertical positions of the tracked particle in blue, with the modeling plotted in red. For particle in figure 15.

3.2.3 Acceleration dependence on the gas flow velocity

The first studied point is the gas flow velocity influence on the experimental acceleration, which directly depends on pressure. The theoretical acceleration of a particle (equation 2) is proportional to the gas velocity v_g, which equals $\frac{r_b \rho_{prop}}{\rho_g}$. r_b is proportional to P^n, and ρ_g with P. The gas flow velocity is proportional to $\frac{r_b}{P}$, or P^{n-1}. Figure 17 shows the median value of all calculated experimental acceleration as a function of the ratio $\frac{r_b}{P}$, for all the experimental runs. Error bars are the 25% and 75% experimental acceleration values.

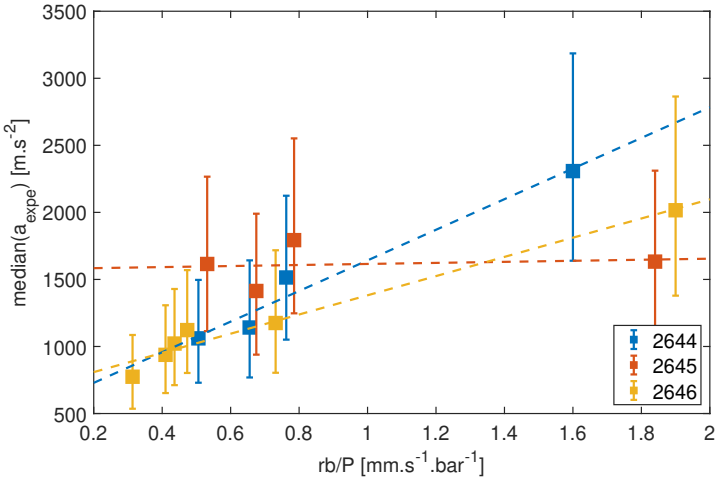

Figure 17: Median experimental acceleration a_{expe} depending on the ratio r_b/P. Dashed lines are the linear regression for each propellant.

The particles acceleration of the 2644 and 2646 propellants seems to be directly proportional to the gas velocity v_g. The particles acceleration of the 2645 seems to be constant, independently of the gas velocity. The 2645 does not include coarse AP particles. They are the only oxidizing particles to form a diffusion flame with the binder at the pressures studied [31]. The influence of the gas temperature may therefore be more important for the 2645 propellant. The influence of the temperature is presented in section 3.3. The error bars are slightly more important with the 2645 propellant, due to the larger discrepancy of the particles size in the gas flow for this propellant.

3.2.4 Acceleration dependence on the particles size

The second studied point is the influence of the particles size on the acceleration. The theoretical acceleration of a particle is proportional to $\frac{1}{D^2}$, with D the diameter of the particle (equation 2). Figure 18 shows a density map of the experimental particles acceleration depending on the inverse of their diameter for the 2644 propellant at 4 *bar*. The function AD^{-k} minimizing the residue $\sum_{i=1}^{N_{part}}(a_{expe} - AD^{-k})$ is also plotted. The exponent k is theoretically equal to 2. Figure 19 shows the exponent k calculated for each experimental run.

As predicted by the theoretical acceleration, the particle size directly drives its acceleration in the gas flow. However, the exponent k decreases with increasing pressure. A possible explanation is the non-homogeneous gas flow

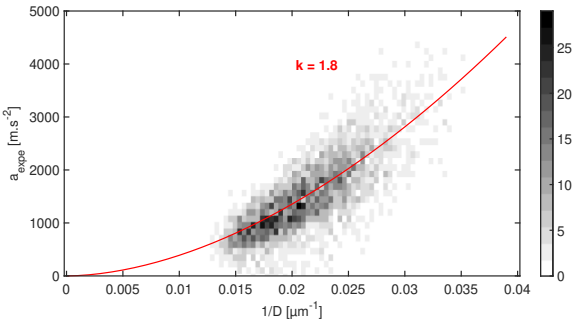

Figure 18: Density map of the experimental acceleration a_{expe} depending on the inverse of the particles diameter D (2644 propellant at 4.0 bar).

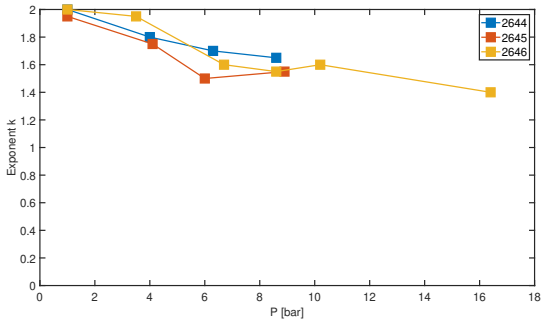

Figure 19: Exponent k of regression law $a_{expe} = AD^{-k}$.

due to the propellant flames. The temperature gradient in the gas flow increases with increasing pressure [31], meaning that the particle thermal expansion may be more important. This is the first visualisation that there is a temperature effect on the drag force F_d.

3.3 Acceleration dependence on the gas temperature

The third studied point is the influence of the temperature. The gas temperature has a direct effect on the theoretical acceleration formulated in equation 2, mainly on two physical parameters:

- μ_g: proportional to $T^{1/2}$.
- $1/\rho_g$: proportional to T.

The theoretical acceleration is proportional to $T^{3/2}$. If T is overestimated, a_{th} is greatly overestimated. All physical values have been calculated in the gas flow assuming the final equilibrium, with the final temperature of the propellant flame T_f. The gas temperature close to the propellant surface where the particle is accelerated is not equal to the final temperature T_f. The gas temperature is somewhat between the surface temperature value and the final equilibrium temperature value. Figures 20 and 21 show the median experimental accelerations a_{expe} depending on the median theoretical accelerations a_{th}. The theoretical accelerations in figure 20 are calculated with the temperature of the equilibrium gas ($T_f = 2350 - 2850\ K$ depending on the propellant and the pressure). The theoretical accelerations in figure 21 are calculated with the temperature of the burning surface ($T_s = 900\ K$ [32]). Error bars are the 25% and 75% acceleration values.

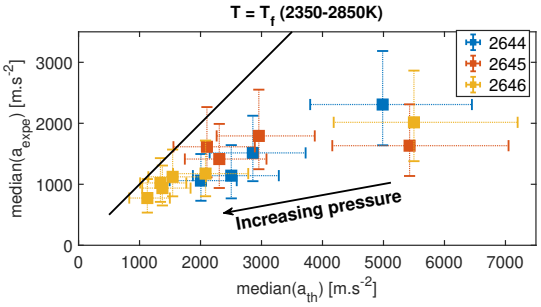

Figure 20: Median experimental acceleration depending on the median theoretical acceleration (calculated with the equilibrium gas temperature), with $y = x$ plotted as reference.

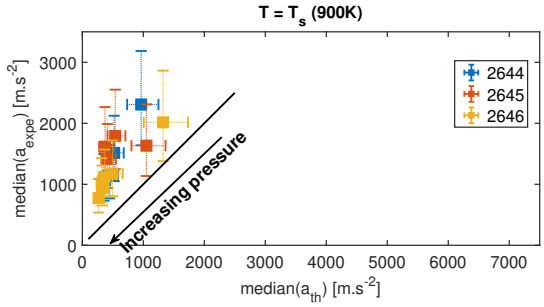

Figure 21: Median experimental acceleration depending on the median theoretical acceleration (calculated with the burning surface temperature), with $y = x$ plotted as reference.

The theoretical acceleration is strongly temperature dependant as seen in figures 20 and 21. The theoretical acceleration is overestimated when calculated with the equilibrium gas temperature T_f, and underestimated when calculated with the surface temperature T_s. The accelerations are lower for the 2646 propellant. This is due to the higher proportion of AP in the propellant mixture and the resulting lower gas temperature.

At high pressures (bottom-left side in figures 20 and 21), theoretical accelerations are close to experimental accelerations when calculated with the equilibrium gas temperature T_f. While at low pressures (top-right side in figures 20 and 21), theoretical accelerations are closer to experimental accelerations when calculated with the burning surface temperature T_s. A possible explanation is the influence of pressure on the temperature field close the burning surface [31]. At low pressures, the gas temperature where particles accelerate is closer to the surface temperature. While at high pressures, the gas temperature is closer to the equilibrium gas temperature. The thermal effect needs to be taken into account for better drag force modeling. The forces modeling are presented in section 4.2, they include a gas temperature modeling. In future works, it could be interesting to determine which temperature value leads to theoretical acceleration levels a_{th} that are consistent with the experimental accelerations a_{expe}.

4. Towards a force-based model

4.1 Pressure influence for experimental agglomeration

The adhesive force and the drag force are studied with the particles uncovering and movement on the surface and their acceleration in the gas flow. The two forces compete with each other when the particle is on the propellant surface. A particle remains attached to the surface when the adhesive force is stronger than the drag force. On the contrary, it leaves the burning surface when the drag force is stronger. The ratio of the two forces influences the level of agglomeration. The aggregates proportion and the agglomerated fraction directly inform on the level of agglomeration. The aggregates proportion P_{agg} is the proportion of tracks discriminated as aggregate, independently of the aggregates size :

$$P_{agg} = \frac{N_{agg}}{N_{agg} + N_{part}} \tag{4}$$

Objects labeled as aggregates contain multiple particles. The number of particles $n(i)$ contained in a tracked aggregate i is approximated by dividing the detected area A by the mean individual particle diameter D_{10} : $n(i) = \frac{4A(i)}{\pi D_{10}^2}$. The estimated number of particles for the aggregate i is averaged on the complete track for all detections to reduce the uncertainty. The agglomerated fraction f_{agg} is the total number of single particles included in all detected aggregates divided by the total number of particles (aggregates + individual particles). It is a way to estimate the proportion of inert particle mass that is found in aggregates:

$$f_{agg} = \frac{\sum_{i=1}^{N_{agg}} n(i)}{\sum_{i=1}^{N_{agg}} n(i) + N_{part}} \tag{5}$$

The aggregates proportion and the agglomeration ratio are calculated for each run. Figure 22 shows the aggregates proportion P_{agg} and figure 23 shows the agglomeration fraction f_{agg} for the three propellants at different pressures.

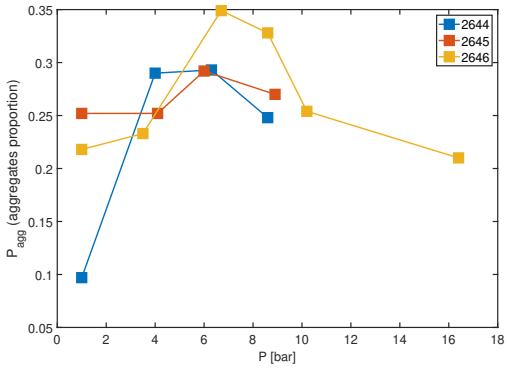

Figure 22: Aggregates proportion depending on pressure, for the 3 propellants studied.

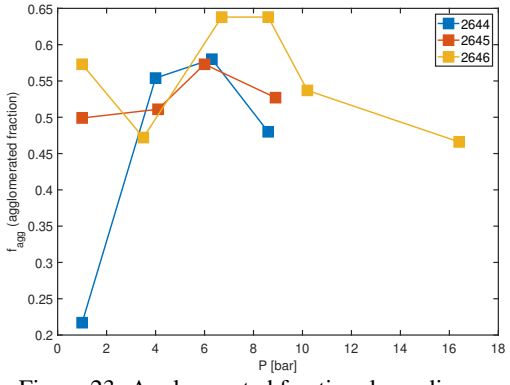

Figure 23: Agglomerated fraction depending on pressure, for the 3 propellants studied.

A clear effect of pressure can be observed. An agglomeration peak is observed for all propellants at the pressure of ≈ 6 *bar*. The inert particles of the 2646 propellant agglomerate the most. However, it was highlighted in section 3.1.3 that those particles are the less retained on the propellant surface and are expected to agglomerate less from an

adhesive force point of view. The explanation of more agglomeration for the 2646 propellant is the less important drag force applied by the propellant, as highlighted from the temperature effect described in section 3.3.

The agglomeration extent depends directly on the adhesive and drag forces comparison. The agglomeration peak at $\approx 6\ bar$ means that the ratio $\frac{F_a}{F_d}$ is maximum at that pressure. Adhesive and drag force models are going to be proposed, they are able to reproduce the experimentally observed agglomeration dependence to pressure.

4.2 Proposed forces modeling

The force models are formulated in order to respect the various experimental observations: the adhesive force is pseudo-binder related, pressure plays a minor role on the adhesive force compared to the granular distribution of AP. The drag force is directly related to pressure via the gas velocity ($v_g \propto P^{n-1}$) and is directly dependant to the gas temperature where the particle is located ($F_d \propto T^{3/2}$). An agglomeration spike is located at the pressure of $\approx 6\ bar$.

The origin of the adhesive force stated in the literature is the liquid layer of carbon-containing residues at the top of the burning surface [16]. Two different adhesive-force models are proposed and discussed. The first is proportional to the wet length l of the particle, the force is similar to a surface tension. The second is proportional to the total surface S of the particle located in the liquid layer. A schematic of two forces is presented in figure 24.

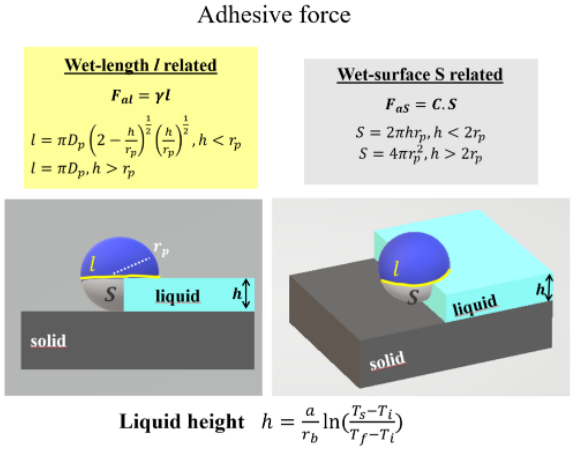

Figure 24: Schematic of the two adhesive-force models.

Concerning the drag force, the theoretical drag force is corrected with pressure and thermal considerations. The theoretical acceleration ($a_{th} = F_d/m_{part}$) is written in equation 2. In the modeling, the correction ($1 + 0.15Re^{0.687}$) is not applied in order to limit the complexity. The drag force is proportional to the gas flow velocity: r_b/ρ_g is proportional to P^{n-1}.

The temperature effect is considered. The drag force evolves with $T^{3/2}$. Here the drag force applied by the gas is studied when the particle is still attached to the surface. The gas temperature close to the pseudo-binder burning surface T_g must be considered, at a distance representative of a particle protrusion. The distance x_g is chosen equal to the representative radius $r_p = D_{10}/2 \approx 20\ \mu m$.

The temperature above the pseudo-binder at this distance is equal to the surface temperature T_s at low pressures ($< 1 atm$), and to the final flame temperature T_f at high pressure (approx. 50 bar) [31]. At intermediate pressures, the final flame temperature T_f is located at a distance x_f from the burning surface, with $x_f \propto r_b$. With a supposed thermal conduction regime, the temperature gradient in the gas is constant, therefore :

$$T_g - T_s = (T_f - T_s)\frac{x_g}{x_f} \tag{6}$$

The gas temperature close to the burning surface T_g is modeled following equation 7, with P in bar and $P_{50} = 50\ bar$. T_f is the final flame temperature, and T_s the pseudo-binder surface temperature.

$$T_g = T_{surf} + \Delta T = T_s + (T_f - T_s)(\frac{P}{P_{50}})^n \tag{7}$$

Therefore the drag force is proportional to the following term:

$$F_d \propto P^{n-1} T_g^{3/2} \propto P^{n-1} [T_{surf} + (T_f - T_{surf})(\frac{P}{P_{50}})^n]^{3/2} \tag{8}$$

An adhesive number A_d is calculated. It is the ratio between adhesive and drag forces (equation 9). It is similar to the Weber number proposed by Kalman et al. [33].

$$A_d = \frac{F_a}{F_d} \tag{9}$$

A_d is calculated on a range of pressure from 1 to 16 *bar* with the properties of the 2644 propellant combustion. Low A_d would result in low inert particles agglomeration. High A_d would result in important agglomeration. The adhesive number is calculated for four cases, presented in table 3. The adhesive force is either proportional to the wet line l or to the wet surface S. The gas temperature effect (equation 7) may be taken into account or not for the drag force, and the thermal diffusivity in the propellant is either equal to the binder HTPB or the pseudo-binder AP-HTPB.

Table 3: Studied cases for adhesive number calculation.

	Case 1	**Case 2**	**Case 3**	**Case 4**
Adhesive force	$\propto l$	$\propto S$	$\propto S$	$\propto S$
Gas temperature effect	No	No	Yes	Yes
Propellant thermal diffusivity a	HTPB	HTPB	HTPB	AP-HTPB

Proprieties of the propellant surface are also required. The pseudo-binder surface temperature is set to 900 K [32] and the initial propellant temperature to 300 K. The thermal diffusivity of the binder HTPB is set to 1.08 10^{-7} $m.s^{-2}$ [34]. The thermal diffusivity of the pseudo-binder is set to 1.47 10^{-7} $m.s^{-2}$, obtained by adding the homogenized AP particles thermal effect [35]. The chosen values are questionable, especially for the thermal diffusivity. It directly depends on temperature and the pseudo-binder composition. The adhesive number A_d of the four cases is plotted in figure 25.

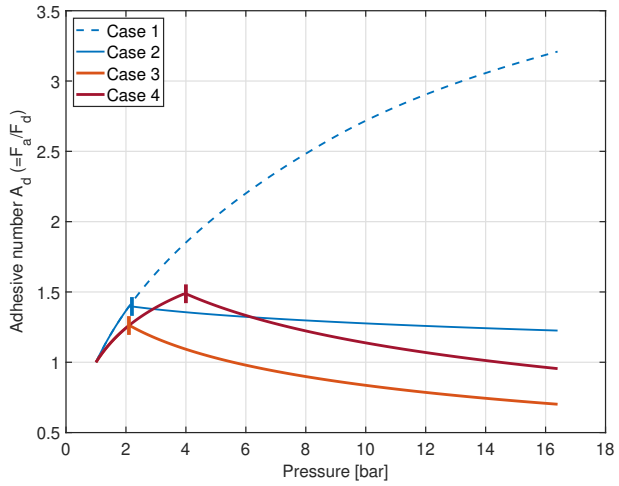

Figure 25: Adhesive number depending on pressure, for the four cases.

An adhesive force proportional to the particle wet surface seems adequate (cases 2 to 4). A maximum of adhesive number A_d is observed. A maximum of A_d number corresponds to a maximum of agglomeration, which is observed experimentally at ≈ 6 *bar*. The adhesive number maximum is located at a pressure depending on the thermal diffusivity. This pressure is the minimum pressure $P*$ for which a particle is not completely covered by the liquid layer. $P*$ increases with the thermal diffusion a, it goes from approximately 2 *bar* to 4 *bar* with only a 36% thermal diffusivity increase. $P*$ is not exactly located at the pressure experimentally observed (≈ 6 *bar*) but the highlighted experimental observation (maximum of agglomeration at an intermediate pressure) is reproduced. Adding a drag force temperature dependence increases the downturn of the adhesive number after the maximum, which is more in agreement with the experimental data (reduction of agglomeration for pressures superior to ≈ 6 *bar*). It is very promising to be able to reproduce experimental variations like that with a first model.

5. Conclusion

This article focused on inert particle agglomeration in solid propellants. This study was carried out with new shadowgraphy images on three different solid propellant compositions between 1 to 16 *bar*. Particles agglomerating on the burning surface are tracked over successive images. The resulting aggregates or individual particles are then tracked as they accelerate in the gas flow. Tracks of detections are classified as particles or aggregates in the gas flow, and the number of particles contained in aggregates is calculated.

Several physical metrics are computed. Those metrics represent the behavior of particles on the propellant surface or in the gas flow. The adhesive force between particles and solid propellant is studied with the protuberance growth and vertical movement of particles on the surface. The drag force applied by the gas flow is studied with the particles acceleration. The overall agglomeration of particles is studied with the aggregates proportion and the agglomerated fraction.

The main experimental observations are the following: the surface retention of particles is mainly driven by the solid propellant granular distribution of medium and large AP, pressure only plays a minor role. The adhesive force is pseudo-binder related. The drag force is proportional to the gas flow velocity, which depends on pressure. The particles drag force depends on their size, with a diameter exponent close to 2 but being pressure-dependant. This observation is explained by the increased thermal gradient above the solid propellant with increasing pressure. The temperature field in the gas flow close to the propellant burning surface has a significant impact on the drag force, and should be modeled. An agglomeration spike is located at the pressure of approximately 6 *bar* for all three propellants studied. Both the adhesive and drag forces diminish with pressure. The drag force diminish more rapidly than the adhesive force up to this pressure, and less rapidly afterwards.

Models of the adhesive and drag force have been proposed based on the experimental observations. An adhesive number, the ratio between the adhesive and drag force is studied. It shows that the proposed modeling would result in an agglomeration dependence to pressure similar to the experiment. The proposed modeling will be implemented in a packing-based numerical simulation code in the near future. The resulting agglomeration will be compared to experimental data, in order to further validate the proposed force models.

6. Acknowledgments

Thomas Decker's PhD is funded by ONERA and ArianeGroup. S. G. thanks DGA (French Procurement Agency) for funding. A special thanks to Aurelie Covasso who helped us for the image annotation. Thanks to Lucie Garagnon, Segolene Palussiere and Albert Grizaut who manufactured the three solid propellants studied in this article.

References

[1] A. Davenas. "Development of modern solid propellants". *Journal of propulsion and power* 19.6 (2003), 1108–1128.

[2] L. T. DeLuca et al. "Microstructure effects in aluminized solid rocket propellants". *Journal of propulsion and power* 26.4 (2010), 724–732.

[3] W. Ao et al. "Aluminum agglomeration involving the second mergence of agglomerates on the solid propellants burning surface: experiments and modeling". *Acta Astronautica* 136 (2017), 219–229.

[4] J. Yuan et al. "Aluminum agglomeration of AP/HTPB composite propellant". *Acta Astronautica* 156 (2019), 14–22.

[5] N. Lupoglazoff et al. "Numerical simulations of the unsteady flow inside segmented solid-propellant motors with burning aluminum particles". In: *40th AIAA Aerospace Sciences Meeting & Exhibit, Reno (USA)*. 2002.

[6] J. Guery et al. "Thrust oscillations in solid rocket motors". In: *44th AIAA/ASME/SAE/ASEE Joint Propulsion Conference & Exhibit, Hartford (USA)*. 2008.

[7] S. Gallier and F. Godfroy. "Aluminum combustion driven instabilities in solid rocket motors". *Journal of propulsion and power* 25.2 (2009), 509–521.

[8] H. Cheung and N. S. Cohen. "Performance of solid propellants containing metal additives". *AIAA Journal* 3.2 (1965), 250–257.

[9] M. Salita. "Deficiencies and requirements in modeling of slag generation in solid rocket motors". *Journal of Propulsion and Power* 11.1 (1995), 10–23.

[10] G. P. Sutton and O. Biblarz. *Rocket propulsion elements, seventh ed.* Wiley, Hoboken, NJ, 2001.

[11] T. Jackson, F. Najjar, and J. Buckmaster. "A new class of agglomeration models for aluminum composite propellants based on random packs". *J. Propul. Power* 21.5 (2005), 925.

[12] M. W. Tanner. *Multidimensional modeling of solid propellant burning rates and aluminum agglomeration and one-dimensional modeling of RDX/GAP and AP/HTPB*. Brigham Young University, 2008.

[13] S. Gallier. "A stochastic pocket model for aluminum agglomeration in solid propellants". *Propellants, Explosives, Pyrotechnics: An International Journal Dealing with Scientific and Technological Aspects of Energetic Materials* 34.2 (2009), 97–105.

[14] J. K. Sambamurthi, E. W. Price, and R. K. Sigman. "Aluminum agglomeration in solid-propellant combustion". *AIAA journal* 22.8 (1984), 1132–1138.

[15] J. Duterque. "Experimental study of the agglomeration of aluminum in solid propellant motors". *ONERA* (1996).

[16] V. A. Babuk, V. A. Vassiliev, and V. V. Sviridov. "Formation of condensed combustion products at the burning surface of solid rocket propellant". *Solid propellant chemistry, combustion, and motor interior ballistics (Progress in Astronautics and Aeronautics)* 185 (2000), 749–776.

[17] E. W. Price and R. K. Sigman. "Combustion of aluminized solid propellants". *Solid propellant chemistry, combustion, and motor interior ballistics (Progress in Astronautics and Aeronautics)* 185 (2000), 663–687.

[18] S. A. Rashkovskii. "Statistical simulation of aluminum agglomeration during combustion of heterogeneous condensed mixtures". *Combustion, Explosion and Shock Waves* 41.2 (2005), 174–184.

[19] M. Plaud and S. Gallier. "A numerical mesoscale model for aluminum agglomeration in solid propellants". In: *7th European Conference for Aeronautics and Space Sciences, Milan (Italy)*. 2017.

[20] T. G. Decker, R. W. Devillers, and S. Gallier. "Experimental visualization of aluminum ignition and burning close to a solid propellant burning surface". In: *European Combustion Meeting 2023, Rouen (France)*. 2023.

[21] R. W. Devillers et al. "Experimental analysis of solid-propellant surface during combustion with shadowgraphy images: new tools to assist aluminum-agglomeration modelling". In: *7th European Conference for Aeronautics and Space Sciences, Milan (Italy)*. 2017.

[22] T. G. Decker, R. W. Devillers, and S. Gallier. "Agglomeration in Solid Propellants loaded with inert particles-Study of physical phenomena using shadowgraphy image processing". In: *9th European Conference For Aeronautics And Space Science, Lille (France)*. 2022.

[23] T. G. Decker, R. W. Devillers, and S. Gallier. "Detecting agglomeration patterns on solid propellant surface via a new curvature-based multiscale method". *Acta Astronautica* 206 (2023), 123–132.

[24] M. Nugue et al. "Particle detection & size evaluation in solid propellant flames via experimental image analysis to improve two-phase flow simulation in rocket motors". In: *Space Propulsion, Seville (Spain)*. 2018.

[25] W. S. Jodrey and E. M. Tory. "Computer simulation of close random packing of equal spheres". *Physical review A* 32.4 (1985), 2347.

[26] S. Gallier and F. Hiernard. "Microstructure of composite propellants using simulated packings and X-ray tomography". *Journal of propulsion and power* 24.1 (2008), 154–157.

[27] T. F. Chan and L. A. Vese. "Active contours without edges". *IEEE Transactions on image processing* 10.2 (2001), 266–277.

[28] J. Matas et al. "Robust wide-baseline stereo from maximally stable extremal regions". *Image and vision computing* 22.10 (2004), 761–767.

[29] J. B. Blaisot and J. Yon. "Droplet size and morphology characterization for dense sprays by image processing: application to the Diesel spray". *Experiments in fluids* 39.6 (2005), 977–994.

[30] G. Welch, G. Bishop, et al. "An introduction to the Kalman filter" (1995).

[31] M. L. Gross and M. W. Beckstead. "Diffusion flame calculations for composite propellants predicting particle-size effects". *Combustion and Flame* 157.5 (2010), 864–873.

[32] J. Powling. "Experiments relating to the combustion of ammonium perchlorate-based propellants". *Symposium (International) on Combustion* 11.1 (1967), 447–456.

[33] J. Kalman et al. "Synchrotron-based measurement of aluminum agglomerates at motor conditions". *Combustion and Flame* 196 (2018), 144–146.

[34] D. M. Hanson-Parr and T. P. Parr. "Thermal properties measurements of solid rocket propellant oxidizers and binder materials as a function of temperature". *Journal of energetic materials* 17.1 (1999), 1–48.

[35] P. Bernigaud, D. Davidenko, and .L Catoire. "A Revised Model of Ammonium Perchlorate Combustion with Detailed Kinetics". *Combustion and Flame* (2023).